Chapter 2
Exploring the Capabilities of Open-Source Hard- and Software for Experimental Dynamics in Rotating Systems

Oliver M. Zobel, Johannes Maierhofer, and Daniel J. Rixen

Abstract This paper presents a first utilization of the Open Acquisition System for IEPE Sensors (OASIS) for experimental dynamic measurements of an academic test structure with a topology similar to a wind turbine designed to have periodically changing mass and stiffness parameters. After deriving the analytical equations of a minimal model, the vibrations of the corresponding test rig are measured using two OASIS boards, one attached to the rotating part and one remaining stationary. Using open-source Python packages, the modes of the system in different configurations are computed and compared to the analytical model. Lastly, the frequency response functions (FRF) for various rotational speeds are retrieved and analyzed. The results show that a complete measurement and analysis process of a mechanical system is possible using mainly open-source hardware- and software. For this reason, the further development of open-source tools, as well as the development of new ones, is desirable.

Keywords Open-Source · Acquisition Hardware · Experimental Dynamics · Experimental Modal Analysis · Operational Vibrations

Introduction

Open-source software brings great advantages; besides being free of charge, it allows everyone to look into the utilized algorithms and adapt the functionality based on individual requirements. For structural dynamics, many noteworthy Python packages exist today, e.g., pyFRF, pyFBS, pyUFF, SDynPy, pyIDI, and many more. The same benefits apply to open hardware, allowing to build on other people's work and customizing for the task at hand. Combining the software side with the steadily increasing amount of open hardware allows the entire measurement and analysis to be performed solely using open tools.

One reason for modifiable data acquisition hardware for the authors was the option to wirelessly synchronize multiple systems because this allows measurements on partly rotating structures, i.e., where one part is rotating while another remains stationary. While commercial systems exist for this purpose, they are too expensive for purely academic investigations. For this reason, the authors developed the Open Acquisition System for IEPE Sensors (OASIS) [1] with a wireless synchronization option.

This paper tests the feasibility of performing a mechanical system analysis using OASIS and open-source software. An academic test structure, with a topology similar to a wind turbine, is used as a test setup. After giving an overview of the test rig, a theoretical model is derived using analytical mechanic principles. The model's behavior is then studied using its eigenvalues and eigenvectors, which depend on the blade angle as well as the blade rotation speed. After detailing the instrumentation used for the test rig, two experimental campaigns are evaluated: A classical experimental modal analysis for different blade angles and an operational analysis for different rotation speeds.

Oliver M. Zobel · Johannes Maierhofer · Daniel J. Rixen
Chair of Applied Mechanics, TUM School of Engineering and Design, Technical University of Munich, Boltzmannstr. 15, 85748 Garching, Germany
e-mail: oliver.zobel@tum.de; j.maierhofer@tum.de; rixen@tum.de

Chad Walber et al. (eds.), *Sensors & Instrumentation and Aircraft/Aerospace Testing Techniques, Vol. 8*, Conference Proceedings of the Society for Experimental Mechanics Series, https://doi.org/10.13052/97887-438-0153-5_2

Test Rig Overview

The test rig analyzed in this paper, shown in fig. 1, was designed to mimic the topology of a wind turbine and is based on an Ampair 600 wind turbine. It consists of three main components: the blade assembly, the nacelle, and the tower with base:

Tower with base Separated from the ground by a spring-based suspension, the tower carries the wind turbine itself. Due to the four springs, the test rig can easily translate up and down as well as tilt around axes perpendicular to the ground. In the following, only the tilting degree of freedom (dof) in the direction of the rotation axis of the wind turbine is considered for this part.

Nacelle The nacelle holds the shaft of the wind turbine, supported by ball bearings and driven by an *Maxon* DC-motor through a planetary transmission and a belt drive. At the end of the shaft, the blade assembly is attached using a bolt and an interlocking socket.

Blade assembly Two blades, comprising of one standard flat-bar steel (cross-section $40 \times 3\,\mathrm{mm}$), are clamped between the two hub discs, denoted as the hub in the following. At the end of each blade, an additional mass m_C is mounted that is designed to increase centrifugal forces.

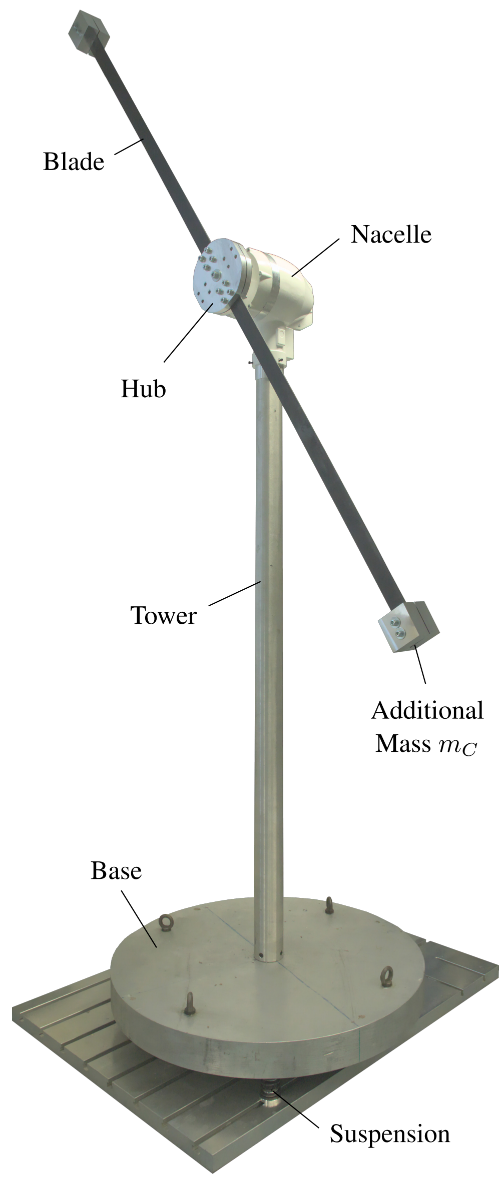

Fig. 1 Overview of wind turbine test rig

Compared to most other wind turbines, the academic test structure only has two blades and, additionally, there is an additional mass m_C attached at the ends of the blades. This design decision was made to amplify the change of system parameters, e.g., mass and stiffness, with a change of the blade angle as well as the rotational speed. For instance, the rotational inertia with respect to the forward tilting of the test rig changes with the blade angle. While this does not apply to wind turbines with three blades in theory, as they can be considered as an isotropic disc (assuming rigid blades), it still applies to imperfect or damaged systems.

Due to the parameters change over time, this system can not be considered Linear Time Invariant (LTI). However, when the rotation speed is kept constant, the system can be regarded as Linear Time Periodic (LTP). Considering this for the modeling process of real systems is relevant because LTP systems can exhibit parametric resonances that are not present in LTI-approximations of the system [2]. However, such effects are not analyzed using the proper LTP system theory in this paper, e.g., by applying Floquet theory as was done in [3].

Here, three selected effects will be modeled using analytical mechanics and the concept of a minimal model. Such a model aims to capture the fundamental physical effects using as few degrees of freedom as possible [4]. The effects specifically modeled are:

Periodic rotational inertia Due to the two blades, the rotational inertia changes proportional to twice the rotational speed. Because the rotational inertia J is identical after a complete revolution or period T_P, assuming constant speed, it is said to be periodic: $J(t + T_P) = J(T_P)$.

Centrifugal stiffening Another effect arises from the rotation speed $\dot{\alpha}$. A mass m traveling on a circular trajectory with constant angular speed $\dot{\alpha}$ and distance to the center r experiences a centrifugal force $F_C = mr\dot{\alpha}^2$, pointing away from the center of rotation. This introduces a prestress in the blades, which results in an increased stiffness for transverse vibrations when $\dot{\alpha} > 0$, which is proportional to the square of $\dot{\alpha}$, as will be shown in the following.

Periodic stiffening and softening through gravity Finally, how gravity affects the system depends on the blade angle α. When the blades are perpendicular to the ground ($\alpha = 0°$), the upper blade experiences a compressive force, while the lower blade experiences a tensile force. This softens or stiffens the blades respectively, analogous to the former effect.

Since the minimal model is supposed to be as simple as possible, the geometry of the test rig is simplified, assuming the tower to be rigid, to an inverted pendulum with one rotational dof, as shown in fig. 2. For this, the mass of the nacelle m_N and the hub m_H are condensed to m_N^*, neglecting the hub length ℓ_H. The mass of the tower m_T is moved to the height of the wind turbine rotation axis $h_T + h_{N,\text{CoR}} = h_T^*$ and adjusted to be of equivalent rotational inertia J at the new position. All modified parameters are denoted by an asterisk superscript, e.g., m_T^*. The determined geometry parameters are summarized in the table in fig. 2c.

For simplicity, any damping in the system is neglected. The masses m_C, m_H, and m_N were determined using a scale; for the blades, generic steel parameters are assumed. Using an experimental modal analysis, the tilting stiffness k_T of the test rig without the hub assembly was identified. Those parameters are included in table 1.

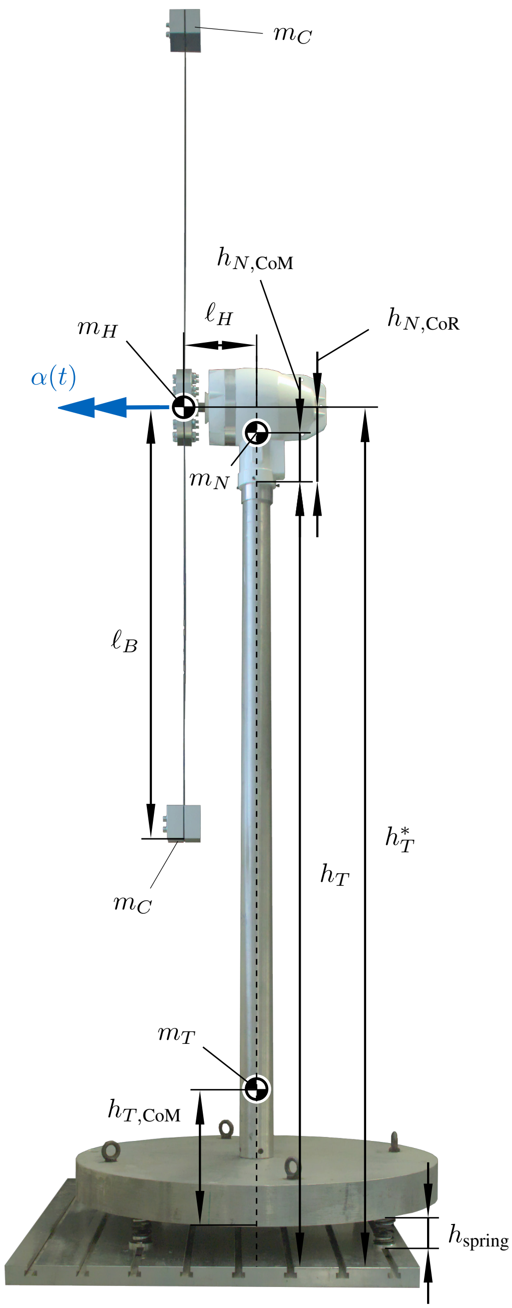

(a) Sideview of test rig with parameter annotations

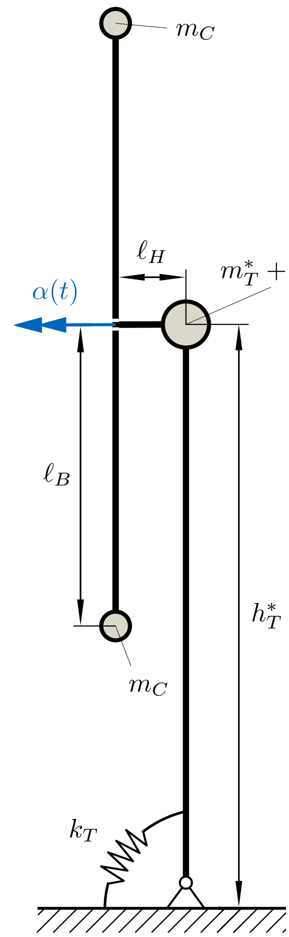

(b) Geometry of minimal model with parameters

Test rig parameter	**Value**
Height of suspension springs h_{spring}	0.07 m
Tower height (including springs) h_T	1.68 m
Nacelle height to center of rotation $h_{N,\text{CoR}}$	0.17 m
Height of wind turbine rotation axis h_T^*	1.85 m
Hub length ℓ_H	0.16 m
Blade length ℓ_B	1.00 m

(c) Wind turbine test rig geometry parameters

Fig. 2 Illustration of test rig geometry and simplification of test rig geometry for minimal model

Theoretical Model

To build a model of the test rig with the aforementioned effects, first, a model of an individual blade using an Euler-Bernoulli beam is derived that considers both the **centrifugal stiffening** as well as the **periodic stiffening and softening through gravity**, which is modeled by an additional, periodic pre-stress. Then, the tower is modeled as an inverted pendulum, to which two of the blade models are connected using primal assembly. Lastly, the **periodic rotational inertia** is added. For the model, the blade angle α and the rotational speed $\dot{\alpha}$ are considered a parameter and not a degree of freedom, i.e., all dynamics relating to a change of α are neglected.

Blade model The derivation starts with the differential equation for an Euler-Bernoulli beam, depicted in fig. 3a, including prestress through a normal force N, which can be found, for instance, in [5]:

$$\rho_B I_B \frac{\partial^2 \ddot{w}_B}{\partial x^2} - \frac{\partial^2}{\partial x^2}\left(E_B I_B \frac{\partial^2 w_B}{\partial x^2}\right) + \frac{\partial}{\partial x}\left(N \frac{\partial w_B}{\partial x}\right) = \bar{m}_B \ddot{w}_B \tag{1}$$

with the beam deflection w_B, density ρ_B, area moment of inertia I_B, Young's modulus E_B and mass per unit length $\bar{m}_B$. The normal force N can now be used to include centrifugal stiffening and periodic stiffening and softening through gravity.

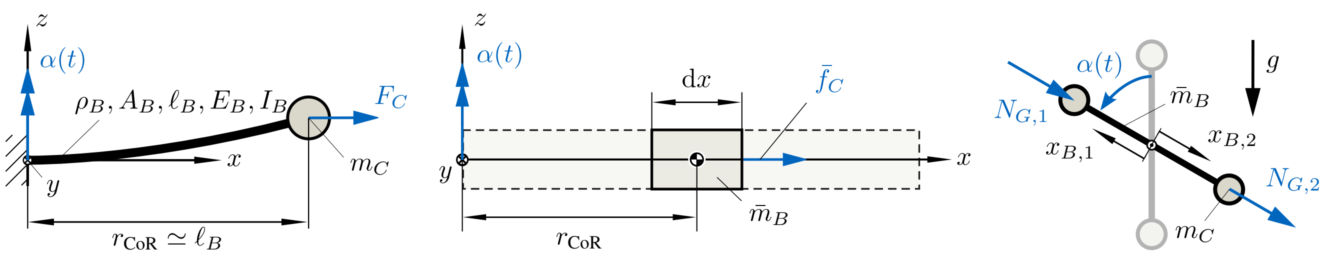

(a) Sketch of Euler-Bernoulli beam with additional blade end mass m_C

(b) Sketch of distributed centrifugal force $\bar{f}_C$ acting on infinitesimal beam mass $\bar{m}_B$

(c) Sketch of normal force N_G introduced by gravity

Fig. 3 Individual modeling steps used for the beam model representing the test rig blades

Centrifugal forces act, on the one hand, on the additional end mass m_C as shown in fig. 3a, and, on the other hand, on the distributed beam mass $\bar{m}_B$ as shown in fig. 3b. In general, the centrifugal force is given by $F_C = m_C r_{\text{CoR}} \dot{\alpha}^2$ with r_{CoR} being the distance to the axis of rotation and $\dot{\alpha}$ the angular velocity. For the end mass m_C, assuming only small deflections w_B and substituting $\dot{\alpha} = 2\pi f_\alpha$, the centrifugal force is then given by $F_C(f_\alpha) = 4\pi^2 \ell_B m_C f_\alpha^2$. For the latter, the distributed centrifugal force $\bar{f}_C$ per distributed mass $\bar{m}_B$ is given as $\bar{f}_C(x) = \bar{m}_B x \dot{\alpha}^2$, which can be integrated over x to the force $\bar{F}_C(x) = \frac{1}{2}\bar{m}_B x^2 \dot{\alpha}^2$, and with the substitution $\dot{\alpha} = 2\pi f_\alpha$ one finds $\bar{F}_C(x) = 2\pi^2 \bar{m}_B x^2 f_\alpha^2$.

The other force acting on the beams is induced by gravity, see fig. 3c. Since the shear force created by gravity acts in the transverse direction orthogonal to the beam deflection direction w_B, it is neglected. Projecting the forces created by gravity onto the beam normal forces yields $N_{G,1,2} = \mp \left(\bar{m}_B \ell_B g \left(1 - \frac{x}{\ell_B}\right) + m_C g\right) \cos\alpha$, with different signs for the two blades. For example, in the upward position with $\alpha = 0$, the first beam is compressed by gravity, and the second beam is elongated.

To summarize, the normal forces $N_{1,2}$ applied to the beams externally is given by:

$$N_{1,2}(x) = \underbrace{4\pi^2 \ell_B m_C f_\alpha^2}_{\text{Centrifugal force due to } m_C} + \underbrace{2\pi^2 \bar{m}_B x^2 f_\alpha^2}_{\text{Centrifugal force due to } \bar{m}_B} \underbrace{\mp \left(\bar{m}_B \ell_B g \left(1 - \frac{x}{\ell_B}\right) + m_C g\right) \cos\alpha}_{\text{Influence of gravity}} \tag{2}$$

In order to be able to get linearized masses and stiffnesses of the beams, a Rayleigh-Ritz ansatz $w_B(x,t) \simeq \boldsymbol{F}(x) \cdot \boldsymbol{q}(t)$, with $\boldsymbol{F}(x)$ being the matrix of shape functions, is made. Using only one shape function $\boldsymbol{F} = \left[\frac{x^2}{\ell_B^2}\right]$ yields the following:

$$K_B(\dot{\alpha}) = E_B \frac{b_B h_B^3}{3\ell_B^3} + \left(\frac{16}{3}\pi^2 m_C + \frac{8}{5}\pi^2 \rho_B b_B h_B \ell_B\right) f_\alpha^2 \mp \left(\frac{4}{3\ell_B} m_c g + \left(\frac{4}{3\ell_B} - 1\right) \bar{m}_B \ell_B g\right) \cos(\alpha) \tag{3}$$

$$M_B = \rho_B b_B h_B \frac{\ell_B}{5} + m_C \tag{4}$$

with the blade thickness b_B and blade height h_B.

Tower model The tower is modeled using an inverted pendulum as depicted in fig. 4a. Writing a rotational equilibrium around the center of rotation yields the equation of motion with respect to ψ, which can be transformed into the translational dof w_T when small angles are assumed.

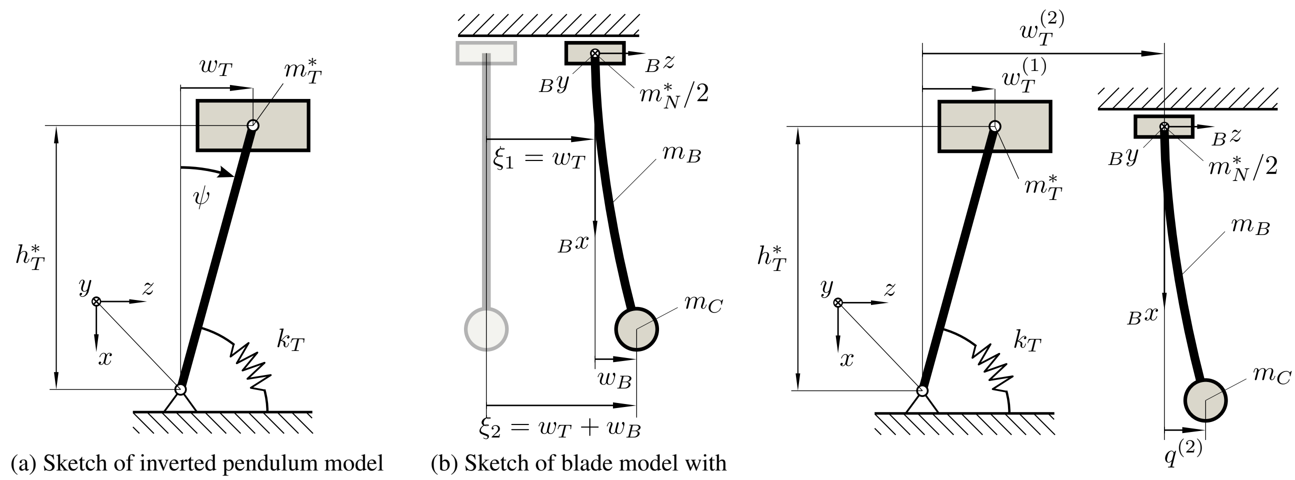

(a) Sketch of inverted pendulum model and kinematics for projection on w_T

(b) Sketch of blade model with additional translation dof

(c) Sketch of the model kinematics for primal assembly

Fig. 4 Individual modeling steps for the tower and extended blade model as well as assembly kinematics

Assembly In order to be able to assemble the beam models to the tower model, the beam model has to be extended with a translational dof as depicted in fig. 4b. The mass of the added dof w_T of the beam model is half of the nacelle mass, which was not considered previously. Using Lagrange's equations, the mass matrix of this extended beam model can be derived:

$$\begin{bmatrix} \frac{m_N^*}{2} + m_C + m_B & \frac{1}{3}m_B \\ \frac{1}{3}m_B & M_B \end{bmatrix} \begin{bmatrix} \ddot{w}_T \\ \ddot{q} \end{bmatrix} + \begin{bmatrix} 0 & 0 \\ 0 & K_B(\dot{\alpha}) \end{bmatrix} \begin{bmatrix} w_T \\ q \end{bmatrix} = \mathbf{0} \tag{5}$$

where $m_B = \rho_B b_B h_B \ell_B$ is the blade mass. No coupling exists between the blade deformation q and the horizontal tower displacement w_T via a stiffness. This is due to the chosen shape function enforcing the boundary condition $w_B(x=0) = 0$, i.e., a displacement q due to a deformation of the beam does not create a displacement of w_T.

Lastly, two extended blade models are assembled to the tower model using primal assembly, see fig. 4c. For this, the horizontal tower displacement $w_T^{(1)}$ has to match the blade displacement $w_T^{(2)}$ of the first blade, requiring $w_T^{(1)} - w_T^{(2)} = 0$. This condition is automatically satisfied by choosing unique global degrees of freedom, here $\boldsymbol{u}_{\text{global}} = \begin{bmatrix} w_T & q_1 \end{bmatrix}^{\mathrm{T}}$. Requiring the same for the second blade (not depicted) yields the assembled system matrices for the global dofs given by $\boldsymbol{u}_{\text{global}} = \begin{bmatrix} w_T & q_1 & q_2 \end{bmatrix}^{\mathrm{T}}$:

$$\boldsymbol{M}_{\text{global}} = \begin{bmatrix} m_T^* + m_N^* + 2m_B + 2m_C & \frac{1}{3}m_B & \frac{1}{3}m_B \\ \frac{1}{3}m_B & M_B & 0 \\ \frac{1}{3}m_B & 0 & M_B \end{bmatrix} \qquad \boldsymbol{K}_{\text{global}} = \begin{bmatrix} \frac{k_T}{{h_T^*}^2} & 0 & 0 \\ 0 & K_B(\dot{\alpha}) & 0 \\ 0 & 0 & K_B(\dot{\alpha}) \end{bmatrix} \tag{6}$$

Periodic rotational inertia The effect of the changing rotational inertia can be added by first deriving the rotational inertia for tilting of the tower with the blades attached depending on the blade angle α. Only considering this change of inertia for the end masses m_C, the total rotational inertia is found as $J_{\text{total}}(\alpha) = (m_T^* + m_N^*)\,{h_T^*}^2 + 2m_C\left(\ell_H^2 + {h_T^*}^2 + \ell_B^2\cos^2(\alpha)\right)$.

Projecting this equation onto the translational dof w_T (by dividing with ${h_T^*}^2$) and comparing the result to the previous diagonal entry of $\boldsymbol{M}_{\text{global}}$ shows that the mass m_C is now multiplied by a changing factor, yielding a periodic contribution:

$$J_{\text{periodic}}(\alpha) = 2m_C\left(\ell_H^2 + {h_T^*}^2 + \ell_B^2\cos^2(\alpha)\right) \quad \leftrightarrow \quad m_C(\alpha) = m_C \cdot \frac{\left(\ell_H^2 + {h_T^*}^2 + \ell_B^2\cos^2(\alpha)\right)}{{h_T^*}^2} \tag{7}$$

Final model Substituting this in the previously found global mass and stiffness matrix yields the final system matrices:

$$\boldsymbol{M}_{\text{global}} = \begin{bmatrix} m_T^* + m_N^* + 2m_B + 2m_C \cdot \dfrac{\left(\ell_H^2 + {h_T^*}^2 + \ell_B^2\cos^2(\alpha)\right)}{{h_T^*}^2} & \dfrac{1}{3}m_B & \dfrac{1}{3}m_B \\ \dfrac{1}{3}m_B & M_B & 0 \\ \dfrac{1}{3}m_B & 0 & M_B \end{bmatrix} \qquad \boldsymbol{K}_{\text{global}} = \begin{bmatrix} \dfrac{k_T}{{h_T^*}^2} & 0 & 0 \\ 0 & K_B(\dot\alpha) & 0 \\ 0 & 0 & K_B(\dot\alpha) \end{bmatrix}$$

$$\text{with} \quad K_B(\dot\alpha) = E_B\frac{b_B h_B^3}{3\ell_B^3} + \left(\frac{16}{3}\pi^2 m_C + \frac{8}{5}\pi^2 m_B\right) f_\alpha^2 \mp \left(\frac{4}{3\ell_B}m_c g + \left(\frac{4}{3\ell_B} - 1\right)\bar{m}_B \ell_B g\right)\cos(\alpha)$$
$$M_B = \frac{1}{5}m_B + m_C \tag{8}$$

All parameters of this model are summarized in table 1. A sketch of the model described by eq. (8) is depicted in fig. 5. Note that this is not a quantitative model, i.e., highly accurate, but only a qualitative model that is supposed to show the dominating mechanical effects of the test rig while also giving insight as to what parameter influences which effect.

Model parameter	**Value**
Model tower height h_T^*	$1.85\,\mathrm{m}$
Hub length ℓ_H	$0.16\,\mathrm{m}$
Blade length ℓ_B	$1.00\,\mathrm{m}$
Blade Young's modulus E_B	$210 \times 10^9\,\frac{\mathrm{N}}{\mathrm{m}^2}$
Blade density ρ_B	$7850\,\frac{\mathrm{kg}}{\mathrm{m}^3}$
Blade height h_B	$3 \times 10^{-3}\,\mathrm{m}$
Blade thickness b_B	$40 \times 10^{-3}\,\mathrm{m}$
Blade area moment of inertia I_B	$9 \times 10^{-11}\,\mathrm{m}^4$
Model tower weight m_T^*	$1.77\,\mathrm{kg}$
Model nacelle weight m_N^*	$8.15\,\mathrm{kg}$
Blade mass per unit length $\bar{m}_B$	$0.942\,\frac{\mathrm{kg}}{\mathrm{m}}$
Blade mass m_B	$0.942\,\mathrm{kg}$
Additional blade end mass m_C	$1\,\mathrm{kg}$
Torsional stiffness k_T	$8.4\,\frac{\mathrm{kN\,m}}{\mathrm{rad}}$

Table 1 Summary of the minimal model parameters

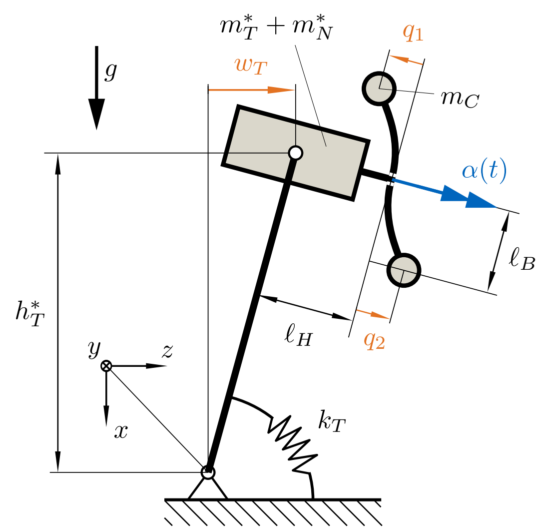

Fig. 5 Coupled, periodic wind turbine minimal model with three degrees of freedom, $\boldsymbol{u}_{\text{global}} = \begin{bmatrix} w_T & q_1 & q_2 \end{bmatrix}^{\mathrm{T}}$

Theoretical Results

To analyze the system behavior, the eigenfrequencies and eigenvectors of the system are calculated using *SciPy*, and the mode shapes are visualized using *Manim* (Mathematical Animation Engine) [6]. The blade angle α and the rotational frequency f_α are substituted by a constant parameter for this. The eigenfrequencies and eigenvectors are then calculated for different values.

Starting with the stationary case, i.e., $\dot\alpha = 0$, the eigenfrequencies and the components of each eigenvector depending on the blade angle α are plotted in fig. 6. In the leftmost plot, the eigenfrequencies are depicted, where the first two eigenfrequencies between 1 and 1.5 Hz belong to the blades, and the third one is mainly a tilting of the tower. As can be seen, all three eigenfrequencies change with the blade angle. For the blades, this change is caused by gravity that compresses or stretches the blades depending on the angle as was derived using fig. 3c. For the tower, the change of eigenfrequency is caused by the change of rotational inertia. Note that this change is proportional to $\cos^2\alpha$, while for the blades, it is proportional to $\cos\alpha$.

One interesting phenomenon is observable with the blade eigenfrequencies: While one would expect the eigenfrequencies to change continuously and proportional to $\cos\alpha$, there appears to be a kink at $\alpha = 90°$. The first eigenfrequency f_1 is defined as the one with the lowest frequency, but this does not mean that it is the same physical eigenfrequency, i.e., that the corresponding mode shape is the same. This can be seen in the eigenvector components in fig. 6.

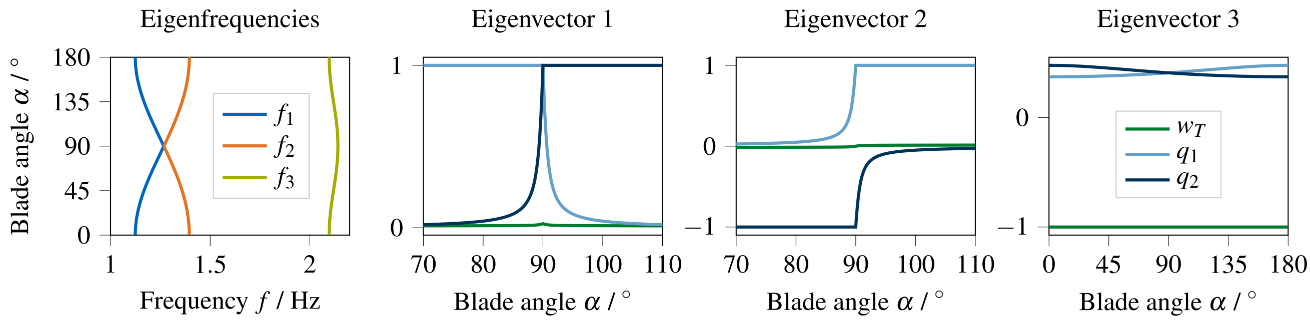

Fig. 6 Evolution of the individual, normalized eigenvectors component over the blade angle α

At $\alpha = 90°$, where both blade eigenfrequencies are identical, it can be seen that the eigenvectors change, i.e., while eigenvector one is dominated by the q_1 component for $\alpha < 90°$, it is dominated by the q_2 component for $\alpha > 90°$. The same can be seen for eigenvector 2, where it changes from q_2 to q_1. This effect is known as mode veering and can generally be observed with systems that have a varying parameter, here the beam stiffness $K_B(\dot{\alpha})$, and are coupled by arbitrarily small amount [7], here through the mass matrix. The rapid change of the eigenvectors in the area where the uncoupled eigenfrequencies cross, as seen here, is typical for mode veering [7].

Visualizing the mode shapes can also provide a physical interpretation of the system behavior. Figure 7 shows the first mode shape for different blade angles, fig. 8 the second mode shape. All mode shape visualizations are created by multiplying the respective normalized eigenvector with $\cos(2\pi t)$ for $t \in [0, 1\,\mathrm{s}]$, scaling the amplitudes by a common factor and applying these values as displacements to the model geometry that is represented to scale. Every figure visualizing mode shapes contains two snapshots of the continuous animation, one with blue and one with orange dots that have a phase of $180°$.

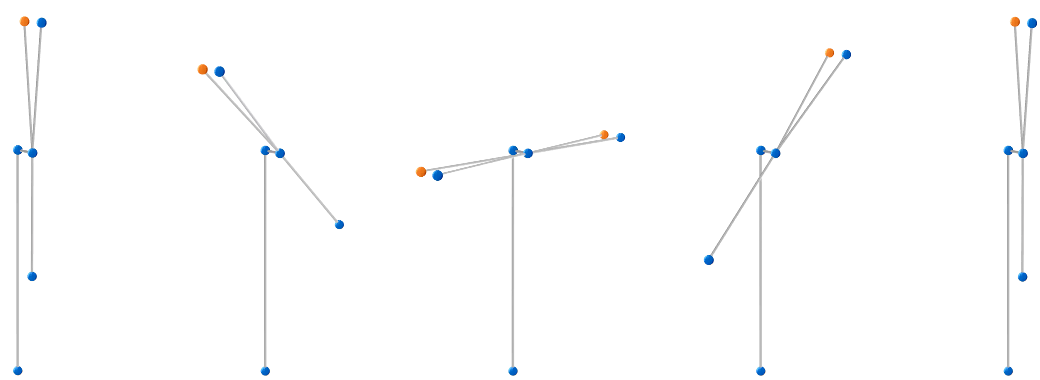

Fig. 7 Mode shape 1 of the minimal model for varying blade angle $\alpha = \{0°, 45°, 90°, 135°, 180°\}$ and $\dot{\alpha} = 0$

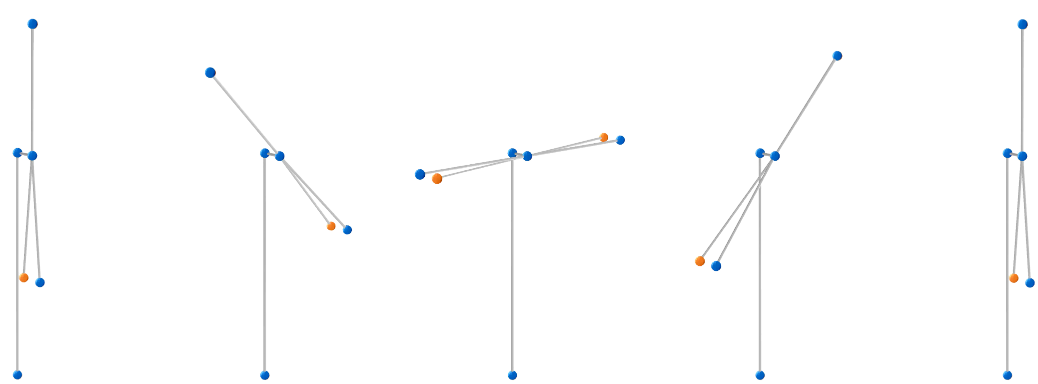

Fig. 8 Mode shape 2 of the minimal model for varying blade angle $\alpha = \{0°, 45°, 90°, 135°, 180°\}$ and $\dot{\alpha} = 0$

The first mode shape, which has the lowest eigenfrequency of the system, always represents the deflection of the upper blade. Since both beams are identical, there is no physical distinction between them. This means that the first mode describes the vibration of beam one for $-90° < \alpha < 90°$ and for $90° < \alpha < 270°$ it describes the vibration of beam two. Both beams vibrate in phase for $\alpha = 90°$. For the second mode shape, the second beam is vibrating for $-90° < \alpha < 90°$ since it has the higher eigenfrequency. At $\alpha = 90°$, both blades deflect in anti-phase, because the eigenvectors have to be linearly independent.

The third mode shape, see fig. 9, describes the tilting of the wind turbine tower coupled with the blade deformation in anti-phase. Because of the periodic stiffening and softening through gravity, the eigenfrequency of the lower beam is always higher, resulting in a higher amplitude in this mode shape since the corresponding eigenfrequency is closer to the third eigenfrequency.

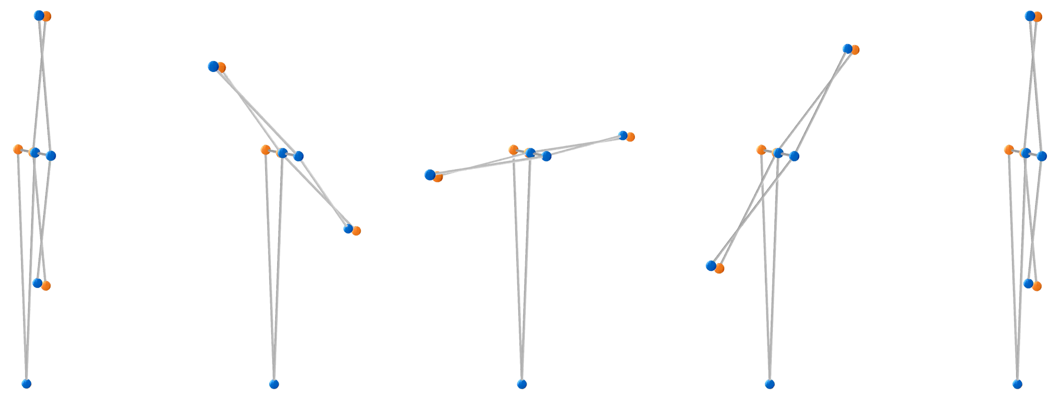

Fig. 9 Mode shape 3 of the minimal model for varying blade angle $\alpha = \{0°, 45°, 90°, 135°, 180°\}$ and $\dot{\alpha} = 0$

Lastly, the system's eigenfrequencies are calculated for different angular velocities $\dot{\alpha}$. The way the minimal model is set up allows to set the blade velocity $\dot{\alpha}$ independently from the blade angle α. An intensity plot is used to show the continuous change of the eigenfrequencies, similar to the phosphor display of analog oscilloscopes. For this, the values of the eigenfrequencies for a large number of angles within one full rotation are plotted over each other with partially transparent lines. This means the more saturated the color is at a specific point, the more often an eigenfrequency is located there, see fig. 10.

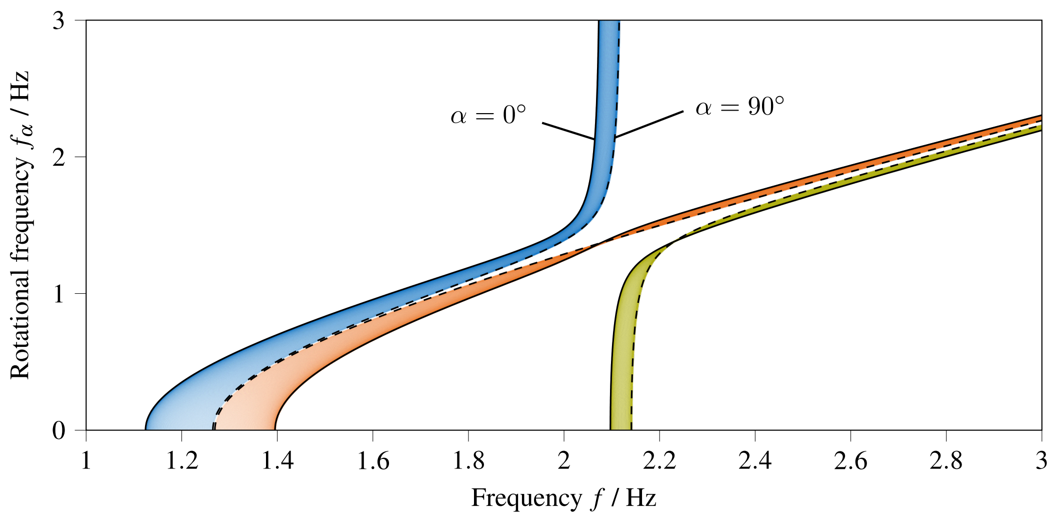

Fig. 10 Intensity plot of the fully assembled model's eigenfrequencies within one full rotation of the blades, for varying rotational blade frequency f_α; the color saturation denotes the rate of the eigenfrequency appearing at the respective point

Also here, mode veering can be observed at the point where the tower eigenfrequency crosses the blade eigenfrequencies. The centrifugal stiffening can also be observed, where the centrifugal forces tension the blades, increasing the stiffness for the transverse vibrations. This leads to an increase of the blade eigenfrequencies when the rotational frequency f_α increases, as can be seen in fig. 10. While this gives an idea of where the linear resonances of the system might be, this does not fully capture the nature of the periodic system that is modeled here. This would require proper modeling as an LTP system [2].

Testrig Instrumentation

Figure 11 shows the wind turbine test rig, including all used instrumentation. Different colors are used for system excitation, sensors, and data acquisition. Dashed lines show the signal flow from sensors to data acquisition. In the following the used components are described in detail. The raw measurement data can also be downloaded from [8].

Excitation The test rig is excited using a shaker attached to the tower with a stinger. Using a waveform generator, random noise with an amplitude of $12\,\mathrm{V}$ peak-to-peak and $30\,\mathrm{MHz}$ bandwidth is created. This signal is fed into a band-pass filter that removes the DC part and most of the higher frequencies using a cut-off frequency of $30\,\mathrm{Hz}$. A gain of $40\,\mathrm{dB}$ is also applied to regain some signal level. This excitation signal is gradually turned on after the measurement begins by controlling the power amplifier's gain, kept at a constant level for approximately $200\,\mathrm{s}$, and then gradually turned off.

The rotational speed of the test rig can be controlled using the DC-motor power supply. There is no control for the actual rotation speed, only a constant voltage can be set. Due to the relatively high rotational inertia, the rotational speed is fairly constant after some settling time.

Sensors Four uniaxial acceleration sensors are glued to the blades, symmetrically to the rotation axis of the wind turbine, such that the distance between the outer sensor and the sensor in the middle of the blade is identical to the distance between the latter and the rotation axis. For $\alpha = 0°$ the test rig is in the configuration as shown in fig. 11, defined by the acquisition system *OASIS One* being oriented with the BNC connectors pointing downwards. The highest sensor in this orientation is denoted as *blade 1 tip*, followed by *blade 1 middle* and *blade 2 middle*, the lowest sensor is denoted *blade 2 tip*.

An impedance sensor between the shaker stinger and the tower measures the force applied by the shaker. A little bit higher up, a triaxial accelerometer measures the acceleration of the tower in the excitation direction. Additionally, the acceleration lateral to the excitation is measured but not further used.

Lastly, the blades' rotation speed, receptively the blades' passing frequency, is sensed using a light barrier. Its circuitry is adapted to be used with a single BNC connection. The supply voltage is provided by the IEPE power supply of the OASIS board. When a blade passes, the LED within the light barrier illuminates, drawing more current than allowed by the limiting circuit (adjusted to $2\,\mathrm{mA}$ from the regular $5\,\mathrm{mA}$). This results in the supply voltage dropping in order to not exceed the set current limit. While the acquisition system can not measure the constant voltage due to the high-pass filter, the change of voltage can be measured. This manifests in voltage spikes with an amplitude of roughly $3\,\mathrm{V}$ that decay moderately fast. These spikes are negative as the blade enters the sensor area and positive as it leaves. Due to the system configuration there are two impulses (four spikes) per complete revolution. A counter, denoted as the blade passing counter, is used to evaluate the rotational frequency during the measurements.

Data acquisition The sensor and excitation signals are digitized using OASIS; specifically, two boards are used. *OASIS One* is attached to the wind turbine hub using a 3D-printed adapter and rotates with the hub. The second system, *OASIS Two*, is stationary. Measurements on this partly rotating system are possible due to the self-contained, Wireless Sample Synchronization (WSS) feature of OASIS, details can be found in [1]. In short, one board, the WSS source, sends a synchronization pulse when the measurement is started. All other boards configured as a WSS sink will start sampling when they receive this pulse. As was shown in [1], the delay between the source and sink measurements is well below $100\,\mathrm{\mu s}$. The samples are transferred to a computer during the measurement using WiFi and UDP, processed, and then saved as *.mat* files.

For all measurements a sample rate of $10\,\mathrm{kHz}$ and a measurement duration of $250\,\mathrm{s}$ was used. In each test rig configuration, five measurements were taken. The channel assignment is summarized in table 2.

Table 2 Summary of channel assignment for the two utilized boards, *OASIS One* and *OASIS Two*

	OASIS One	OASIS Two
Channel 1	Acceleration sensor blade 1 tip	Impedance sensor (force)
Channel 2	Acceleration sensor blade 1 middle	Light barrier signal
Channel 3	Acceleration sensor blade 2 middle	Acceleration sensor in excitation direction
Channel 4	Acceleration sensor blade 2 tip	Acceleration sensor in direction lateral to excitation

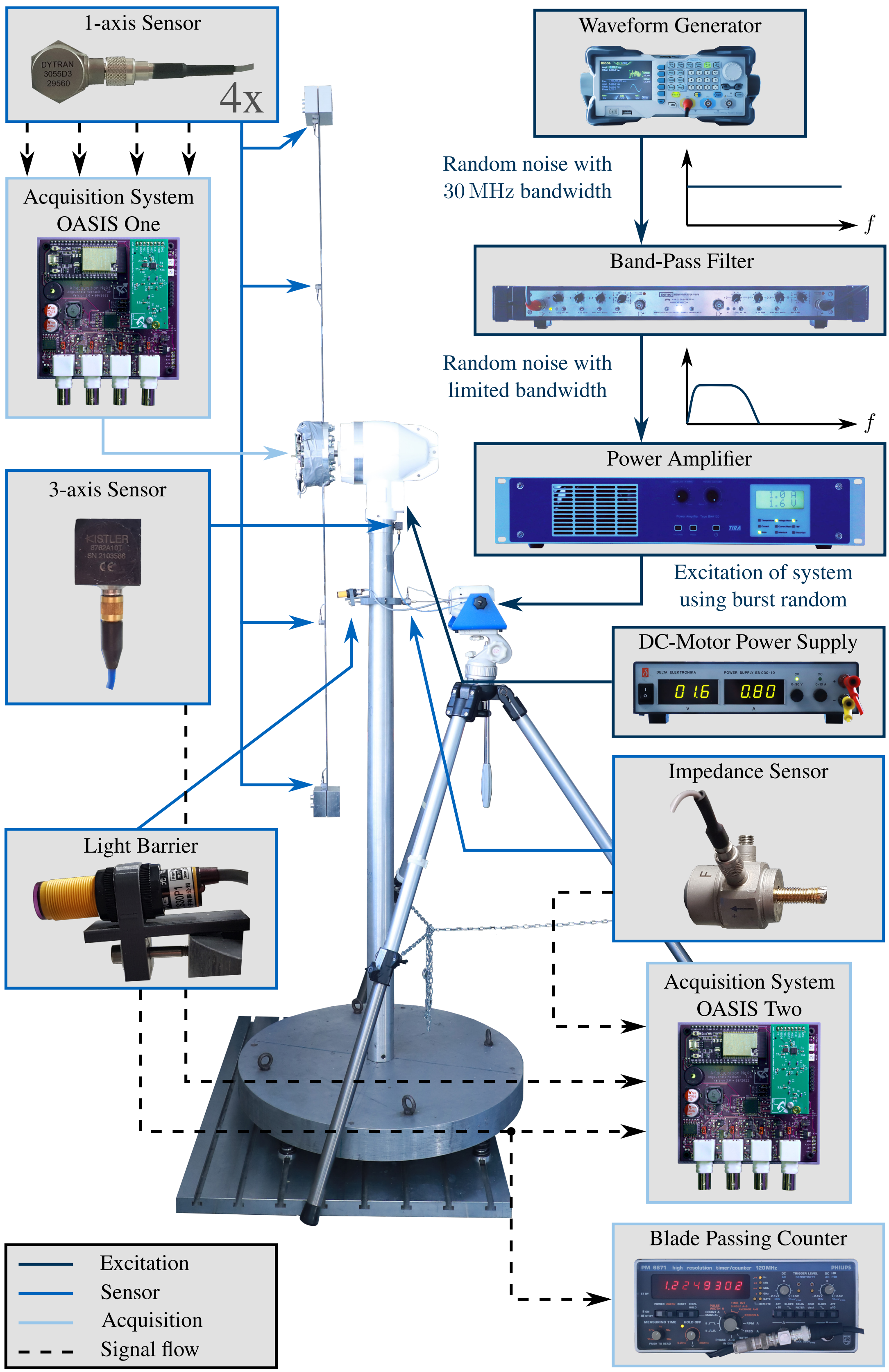

Fig. 11 Illustration of the used test rig instrumentation and signal flow from sensors to acquisition systems

Experimental Modal Analysis

For the stationary measurements used here, the blade angle α was varied between 0 and 180° with 30° increments. From the raw time signals, available at [8], the frequency response functions (FRF) from the shaker excitation to the tower degree of freedom as well as the four blade dofs were calculated with *pyFRF* [9] using five averages and the H_1 estimator. The FRFs of the tower dof for various blade angles α are shown in fig. 12.

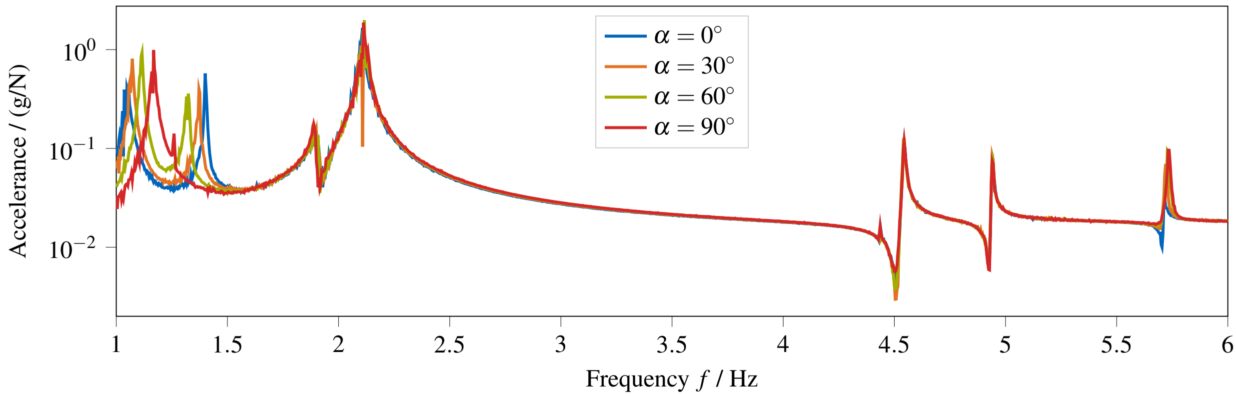

Fig. 12 Plot of the FRF corresponding to the tower degree of freedom for different blade angles α

The greatest variation with the blade angle α can be seen for the two eigenfrequencies around 1 Hz, which belong to the two blades. Slight changes can be seen as well with the two eigenfrequencies around 2 Hz and the eigenfrequency around 5.7 Hz.

For further analysis, the eigenfrequencies f_i, damping ratios ϑ_i and mode shapes are identified using the *pyFBS* [10] implementation of the least-squares complex frequency-domain estimator [11]. Table 3 summarizes the estimated parameters for the different blade angles. To visualize the change of eigenfrequencies and damping rations, the cells in table 3 are colored green if the parameter increased compared to the measurement at $\alpha = 0$ and are colored red for decreasing values.

The most apparent change of eigenfrequency can be seen for modes one and two that behave as predicted by the minimal model, i.e., f_1 increasing as the compression of blade 1 due to gravity is reduced and f_2 decreasing. For the tilting tower mode shape, presumably mode 3 or 4, no significant trend is visible. The higher frequencies are not covered by the minimal model. Mode 5 and 6 appear to be invariant with respect to α, while mode 7 shows slight variations with the blade angle α.

Mode		$\alpha = 0°$	$\alpha = 30°$	$\alpha = 60°$	$\alpha = 90°$	$\alpha = 120°$	$\alpha = 150°$	$\alpha = 180°$
Mode 1	f_1	1.049 Hz	1.070 Hz	1.112 Hz	1.165 Hz	1.139 Hz	1.092 Hz	1.059 Hz
	ϑ_1	0.51 %	0.37 %	0.34 %	0.25 %	0.27 %	0.26 %	0.43 %
Mode 2	f_2	1.402 Hz	1.371 Hz	1.321 Hz	1.259 Hz	1.290 Hz	1.339 Hz	1.390 Hz
	ϑ_2	0.23 %	0.22 %	0.25 %	0.24 %	0.29 %	0.31 %	0.27 %
Mode 3	f_3	1.904 Hz	1.902 Hz	1.904 Hz	1.891 Hz	1.894 Hz	1.888 Hz	1.895 Hz
	ϑ_3	0.75 %	0.65 %	0.56 %	0.59 %	0.52 %	0.75 %	0.71 %
Mode 4	f_4	2.108 Hz	2.111 Hz	2.112 Hz	2.112 Hz	2.112 Hz	2.105 Hz	2.106 Hz
	ϑ_4	0.40 %	0.49 %	0.45 %	0.77 %	0.41 %	0.33 %	0.44 %
Mode 5	f_5	4.544 Hz	4.543 Hz	4.541 Hz	4.543 Hz	4.543 Hz	4.544 Hz	4.542 Hz
	ϑ_5	0.11 %	0.10 %	0.11 %	0.12 %	0.11 %	0.11 %	0.12 %
Mode 6	f_6	4.941 Hz	4.940 Hz	4.940 Hz	4.939 Hz	4.940 Hz	4.941 Hz	4.941 Hz
	ϑ_6	0.06 %	0.06 %	0.06 %	0.07 %	0.05 %	0.06 %	0.06 %
Mode 7	f_7	5.712 Hz	5.720 Hz	5.729 Hz	5.734 Hz	5.731 Hz	5.721 Hz	5.712 Hz
	ϑ_7	0.06 %	0.07 %	0.08 %	0.08 %	0.08 %	0.09 %	0.10 %

Table 3 Summary of identified eigenfrequencies f_i and damping ratios ϑ_i for the wind turbine test rig at standstill; coloring shows trend of parameters compared to measurement at $\alpha = 0°$ (green = increasing, red = decreasing)

For the experimentally identified mode shapes, *Manim* [6] was also used to create visualizations. The first two mode shapes are displayed in fig. 13 and fig. 14. As with the minimal model, mode shape 1 describes the deflection of the upper blade, and mode shape 2 the deflection of the lower blade. At $\alpha = 90°$, both blades vibrate in phase for mode 1 and in anti-phase for mode 2. Except for some slight deflections of the opposing blade, the experimental mode shapes match the model.

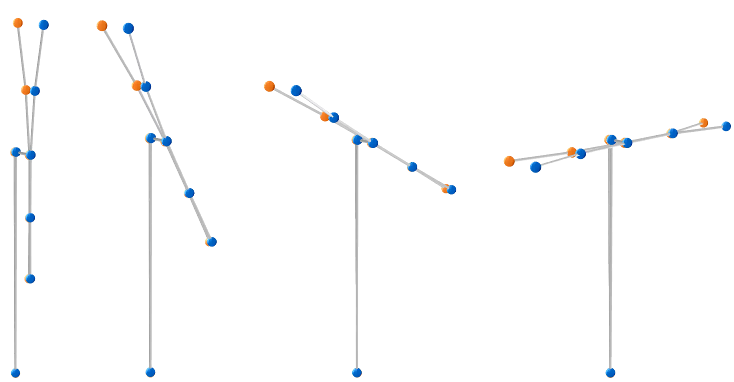

Fig. 13 Test rig mode shape 1 - Upper blade deformation - for $\alpha = \{0°, 30°, 60°, 90°, 120°, 150°, 180°\}$

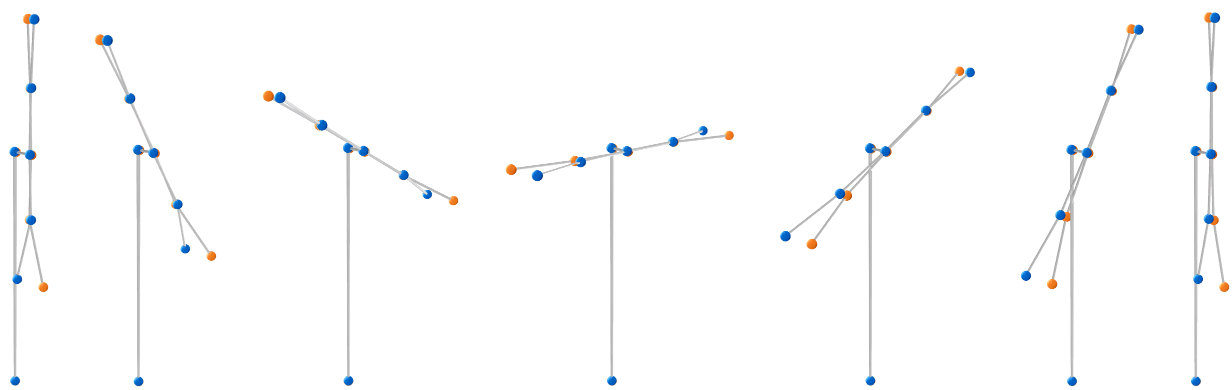

Fig. 14 Test rig mode shape 2 - Lower blade deformation - for $\alpha = \{0°, 30°, 60°, 90°, 120°, 150°, 180°\}$

For the third mode shape of the model, the tilting of the tower, there exist two candidates from the experiments, mode shape 3 (fig. 15) and mode shape 4 (fig. 16). With the utilized dofs, there is no distinction possible. Calculating the values of the Auto Modal Assurance Criterion (Auto-MAC) also reveals a very high dependence ($\approx 96\,\%$) of the modes 3 and 4. Besides that, both mode shapes also show the same vibration behavior as the third mode shape of the model, i.e., the tower dof exhibits displacements in one direction, while all blade dofs move in the opposite direction.

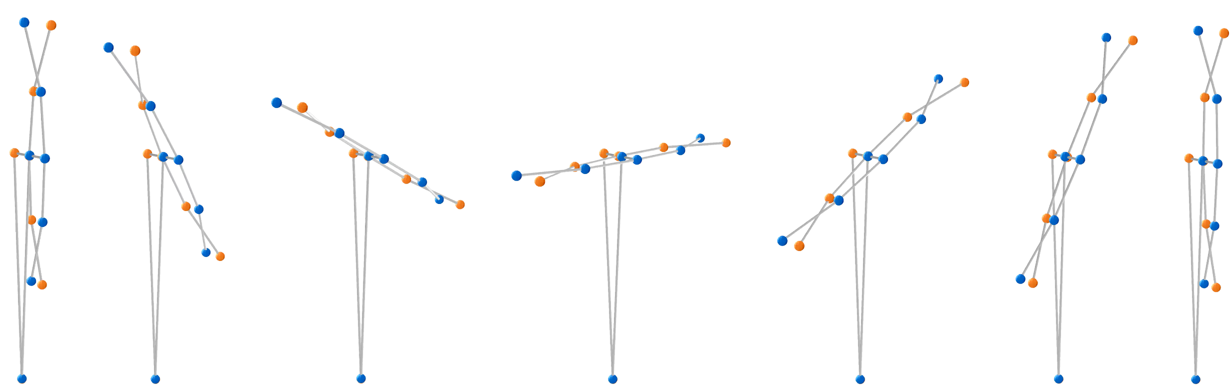

Fig. 15 Test rig mode shape 3 - Tilting tower multiplicity 1 - for $\alpha = \{0°, 30°, 60°, 90°, 120°, 150°, 180°\}$

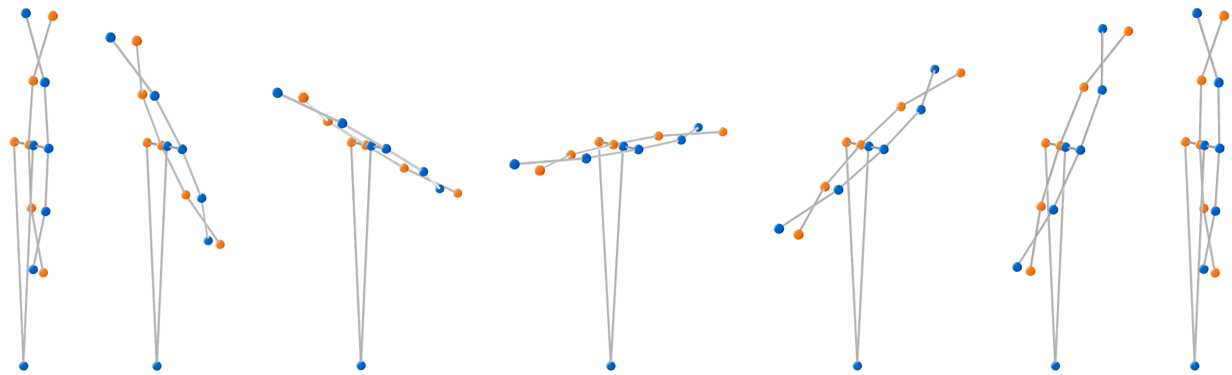

Fig. 16 Test rig mode shape 4 - Tilting tower multiplicity 2 - for $\alpha = \{0°, 30°, 60°, 90°, 120°, 150°, 180°\}$

The fifth and sixth experimental mode shapes behave very similar to the previously described ones and also show a moderately high Auto-MAC value ($\approx 55\,\%$) and are therefore not shown here. Lastly, the seventh mode shows a second-order bending mode of the blades, see fig. 17. Since this mode shape is focused on the blades, the frequency dependence can probably also be explained by the stiffening/softening effect due to gravity.

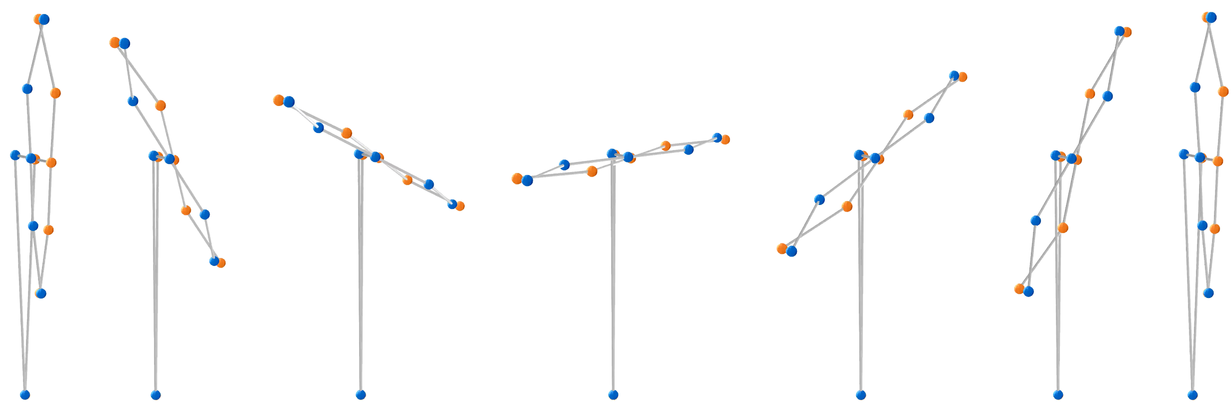

Fig. 17 Test rig mode shape 7 - Higher Order Blade Deformation - for $\alpha = \{0°, 30°, 60°, 90°, 120°, 150°, 180°\}$

Finally, the values of the modeled and experimentally identified eigenfrequencies are compared using fig. 18. The eigenfrequencies of the blades (blue and orange) correspond pretty well and show the same qualitative change with the blade angle α. At the point with $\alpha = 90°$, where the eigenfrequencies should be identical, there is a difference of about $0.1\,\text{Hz}$. Since mode veering occurs in a region around the critical points, that is in the order of the off-diagonal terms that couple the individual degrees of freedom [7], this implies that the model might be missing some coupling terms. Also, neither of the two experimentally identified tower tilting eigenfrequencies show a dependence on the blade angle α as suggested by the theoretical model. The second identified tower tilting eigenfrequency is most likely a sideways motion of the tower, not covered by the model.

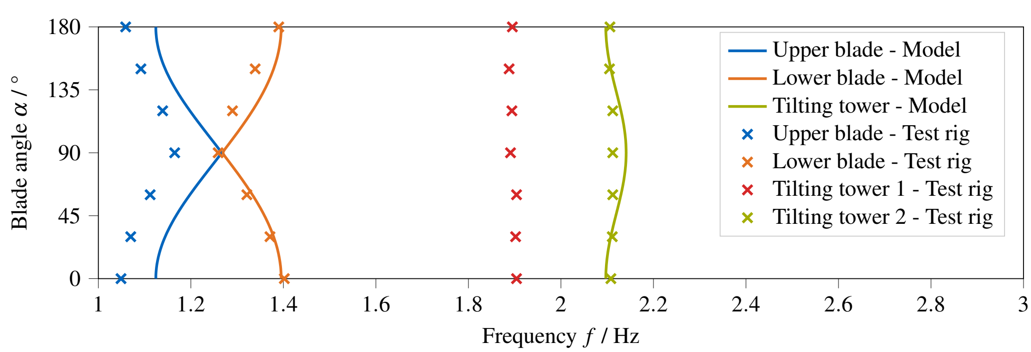

Fig. 18 Plot of the modeled and the experimentally identified eigenfrequencies for varying blade angle α with $\dot{\alpha} = 0$

Operational Measurements

Next, the dynamic measurements with $\dot{\alpha} \neq 0$ shall be analyzed. Measurements were taken for rotational frequencies f_α in 0.1 Hz steps, from 0.1 Hz to 1.2 Hz, whereby no measurements were taken for 1.0 Hz since the test rig exhibited a resonance at this rotational frequency. During the dynamic measurements the system was also excited by the shaker with burst random. For the evaluation, FRFs are calculated using *pyFRF* [9]. However, no modal parameters are extracted due to the high amount of noise and because the system can not be considered time-invariant. The rotational frequency f_α was set during the measurements using the DC-motor power supply and checked using the blade passing counter as depicted in fig. 11. Using peak detection on the light barrier signal, the average rotational frequency can be calculated.

For the plots of the dynamic results, the desired frequency f_α is used. However, note that due to some deviations of the average frequencies, especially for 0.3 and 0.4 Hz, there might be some distortion. The spectrograms are created using *Matplotlib*'s *imshow* command, which interpolates the plots. This can especially be noticed around $f_\alpha = 1$ Hz, where no measurement data exists. To start the analysis of the system's behavior, the FRF trace, i.e., the sum of all diagonal entries of the FRF matrix, for each measured rotational frequency is plotted in fig. 19. The x-axis represents the frequency axis of the FRFs for each rotational frequency f_α, starting with the FRF for $f_\alpha = 0.1$ Hz at the bottom to the one on the top for $f_\alpha = 1.2$ Hz.

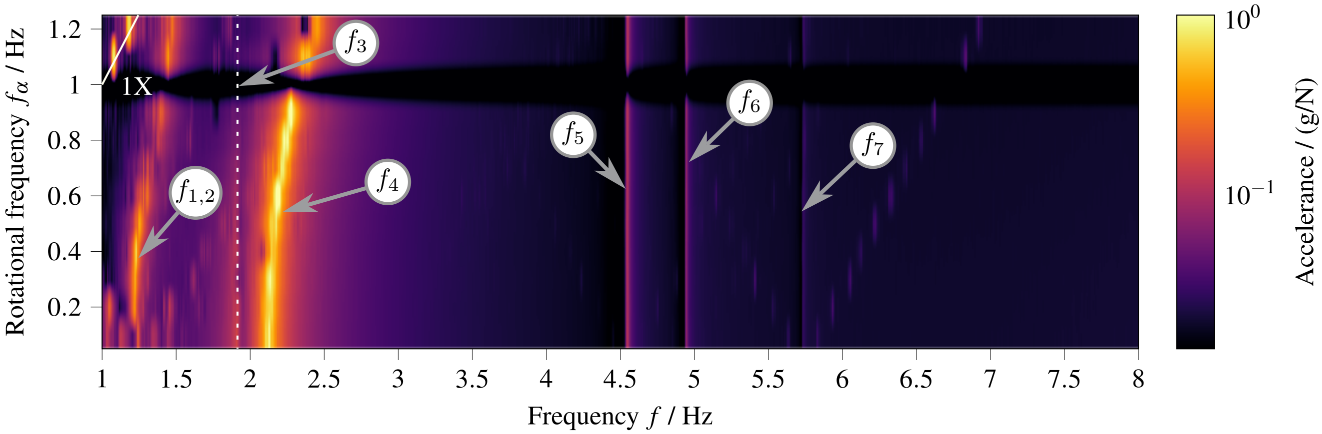

Fig. 19 Spectrogram showing the **FRF Traces** for different rotational frequencies f_α with eigenfrequencies f_i annotated

Visible most clearly are the eigenfrequencies of the two blades $f_{1,2}$ that merged to one line and one of the eigenfrequencies belonging to the tower, namely f_4, while f_3 is only faintly visible. All three of those eigenfrequencies, not including f_3, show a clear dependence on the rotational frequency and increase with f_α. Also clearly visible is the first excitation order, marked as 1X, due to some unbalance. The higher eigenfrequencies are less pronounced and are constant. One interesting effect can be seen for f_7, the second-order beam deformation, which is only visible in the FRFs corresponding to the blade

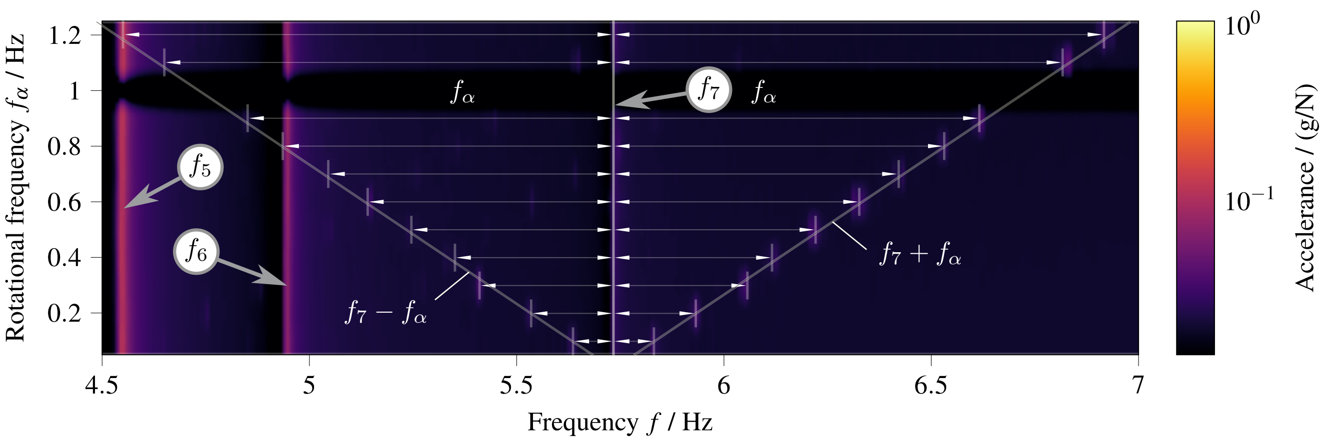

Fig. 20 Magnified spectrogram showing the **FRF Traces** for different f_α within 4.5-7 Hz

acceleration sensors. While the eigenfrequency is constant, there are sidebands that have an increasing distance to f_7 for higher rotational frequencies. This part of the plot is enlarged in fig. 20 and analyzed in more detail.

In fig. 20, there are two lines denoting the frequencies $f_7 - f_\alpha$ and $f_7 + f_\alpha$ as well as vertical lines marking the aforementioned quantities for the actual rotational frequency f_α during the measurements. As can be seen, the sidebands are exactly spaced by f_α from the eigenfrequency f_7. The presence of these sidebands at a distance equal to an integer multiple of the fundamental frequency, here the rotational frequency f_α, is a consequence of the periodic system behavior and typical for LTP-systems [12]. Here, the periodically changing parameter is most likely the stiffness of the blades due to gravity.

A closer look shall also be taken at the lower eigenfrequencies the minimal model covers. The appropriate segment from 1 to 3 Hz is shown in fig. 21. Similar sidebands can also be found for the blade mode shapes $f_{1,2}$, although the distance from the dominant peak does not equate to an integer multiple of f_α. Tracing the respective average rotational speed from the visible sideband peaks toward the location of the beam eigenfrequencies $f_{1,2}$ leads to what is shown in fig. 21.

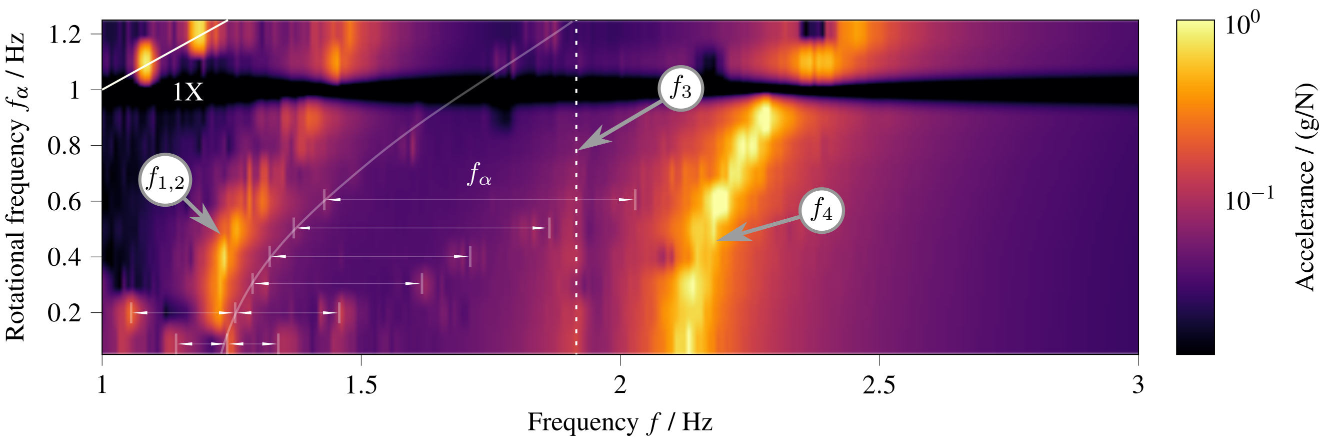

Fig. 21 Magnified spectrogram showing the **FRF Traces** for different f_α within 1-3 Hz

The sidebands have a distance equal to an integer multiple of the average rotational frequency f_α, but not to the visible blade eigenfrequencies $f_{1,2}$ and instead to other sporadic peaks, traced with a bent line. This line also corresponds to an antiresonance visible in the FRFs of the tower, see fig. 22. Since the system is excited at the tower, fig. 22 shows a driving point FRF. At the antiresonance frequency, by definition, the tower does not exhibit any movement and only the attached system, the blade assembly, vibrates at its eigenfrequency. The sidebands are visible at a distance equal to an integer multiple of the average rotational frequency when measured from the uncoupled eigenfrequencies of the periodically varying system.

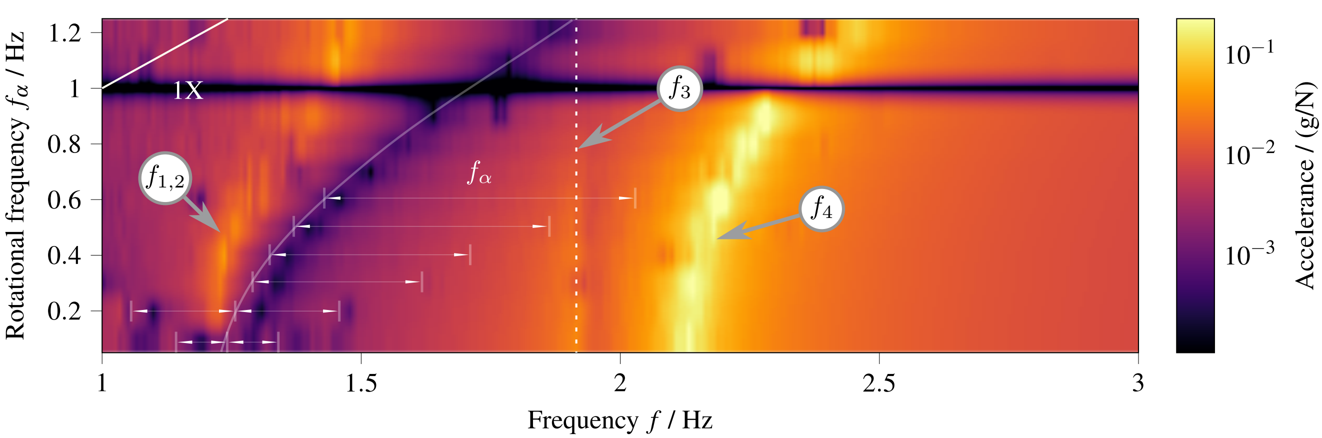

Fig. 22 Spectrogram showing the FRFs of the **Tower** for different f_α within 1-3 Hz

Lastly, the agreement of the minimal model and the experimental results shall be assessed. Since the minimal model's behavior with varying rotational frequency f_α was determined by calculating eigenfrequencies at fixed values for the blade angle α and rotational speed $\dot{\alpha}$, essentially linearizing the system around this configuration, no behavior typical for LTP-systems can be analyzed with the model. Therefore, the only possible comparison is between the values of the modeled eigenfrequencies for all angles α and the basically averaged eigenfrequencies observed experimentally and how they develop with the rotational frequency f_α. For this, the intensity plot of the minimal model is plotted over the spectrogram of the FRF traces, see fig. 23.

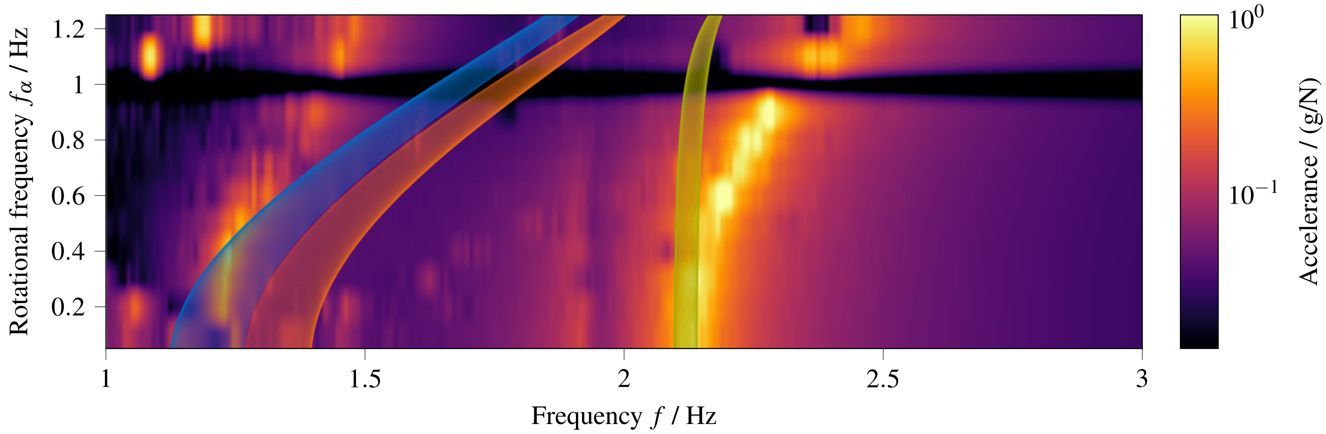

Fig. 23 Magnified spectrogram showing the **FRF Traces** and model intensity plot for different f_α

The agreement with the minimal model is not very good for higher rotational frequencies f_α. Since the blade assembly has an angular momentum for rotational speeds $\dot{\alpha} \neq 0$, a displacement of the tower requires a tilting of the rotation axis. Due to gyroscopic effects, with an increase of the rotational frequency f_α, there is an increasing resistance against the tower tilting that increases the eigenfrequency. This was not considered in the minimal model. Also, the eigenfrequencies of the blades are off and become too stiff for higher rotational frequencies f_α. Looking at the tower FRFs in fig. 24, the agreement of the model's blade eigenfrequencies with the antiresonance frequency/frequencies, i.e., when the tower is fixed, is pretty good, implying that the coupling between the blades and the tower is not modeled precisely enough.

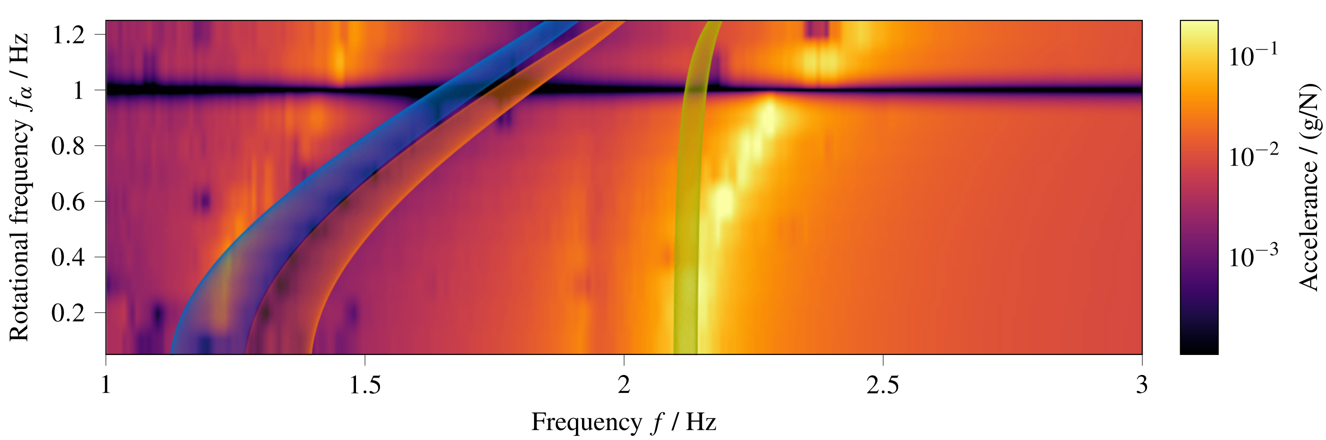

Fig. 24 Magnified spectrogram showing the FRFs of the **Tower** and model intensity plot for different f_α

Conclusion and Outlook

While the utilized minimal model could not fully capture the dynamics observed for the test rig, mainly because some effects were missed in the modeling processes, it was still able to predict most of the quantitative behavior. If the minimal model were to be updated, a sideway degree of freedom should be added to the tower to allow representing gyroscopic effects on the global system dynamics. The true experimental dynamics could be analyzed here using the measured vibrations on both the tower and the blades during rotation. While no LTP-theory was applied here, an evaluation of the existing data [8] might be interesting.

Building on preexisting open-source tools enabled the analysis of this academic test rig, both quickly and cost-effectively. While open-source tools cannot replace commercially available tools in all circumstances, here, no noticeable limitations were found. Another big advantage is the openness and adaptability, which are vital for enabling the quick development of new measurement procedures or evaluation techniques within academia. For this reason, the further development of available open-source tools, as well as the development of new ones, is desirable. Therefore, the authors decided to further develop the *Open Acquisition System for IEPE Sensors* and build an improved version, called *OASIS-UROS: Open Acquisition System for IEPE Sensors - Upgraded, Refined, and Overhauled Software*, which is further detailed in [13].

References

[1] Zobel, O. M., Maierhofer, J., and Rixen, D. J. "OASIS: Open Acquisition System for IEPE Sensors: For Academic Research and Teaching Purposes". In: *Conference Proceedings of the Society for Experimental Mechanics Series* (2024), pp. 79–86. DOI: 10.1007/978-3-031-34938-6_9.

[2] Allen, M. S. "Frequency-Domain Identification of Linear Time-Periodic Systems Using LTI Techniques". In: *Journal of Computational and Nonlinear Dynamics* 4.4 (2009). ISSN: 1555-1415. DOI: 10.1115/1.3187151.

[3] Allen, M. "Floquet Experimental Modal Analysis for System Identification of Linear Time-Periodic Systems". In: International Design Engineering Technical Conferences and Computers and Information in Engineering Conference Volume 5: 6th International Conference on Multibody Systems, Nonlinear Dynamics, and Control, Parts A, B, and C (2007). DOI: 10.1115/DETC2007-34790.

[4] Dresig, H. and Holzweißig, F. *Dynamics of Machinery: Theory and Applications*. Springer Berlin Heidelberg, 2010. ISBN: 9783540899402.

[5] Géradin, M. and Rixen, D. J. *Mechanical vibrations: theory and application to structural dynamics*. 3rd. John Wiley & Sons, Ltd, 2014. ISBN: 978-1-118-90020-8.

[6] The Manim Community Developers. *Manim – Mathematical Animation Framework*. Version v0.17.2. 2022. URL: https://www.manim.community/.

[7] Mace, B. and Manconi, E. "Mode veering in weakly coupled systems". In: *Proceedings of ISMA2012-USD2012* (2012).

[8] Zobel, O. M., Maierhofer, J., and Rixen, D. J. *Rotating System Measurements using the Open Acquisition System for IEPE Sensors (OASIS)*. Dataset. 2024. DOI: 10.14459/2024mp1752772.

[9] Slavič, J., Česnik, M., Zaletelj, K., and Novak, L. *pyFRF: Frequency response function as used in structural dynamics (v0.40)*. 2019. URL: https://github.com/ladisk/pyFRF.

[10] Bregar, T., El Mahmoudi, A., Kodrič, M., Ocepek, D., Trainotti, F., Pogačar, M., and Göldeli, M. *pyFBS (v0.2.9)*. 2022. URL: https://pyfbs.readthedocs.io/en/latest/index.html.

[11] Guillaume, P., Verboven, P., Vanlanduit, S., Van der Auweraer, H., and Peeters, B. "A poly-reference implementation of the least-squares complex frequency-domain estimator". In: *Proceedings of IMAC XXI* (2003).

[12] Tcherniak, D. and Allen, M. "Experimental characterization of an operating Vestas V27 wind turbine using harmonic power spectra and OMA SSI". In: May 2015.

[13] Zobel, O. M., Maierhofer, J., Köstler, A., and Rixen, D. J. "OASIS-UROS: Open Acquisition System for IEPE Sensors - Upgraded, Refined, and Overhauled Software". In: *HardwareX* (2025). ISSN: 2468-0672. DOI: 10.1016/j.ohx.2025.e00650.